Annu. Rev. Fluid Mech. 2001. 33:93–127

EXPERIMENTS ON THERMOCAPILLARY INSTABILITIES

Michael F Schatz[1] and G Paul Neitzel[2]
[1]*School of Physics,* [2]*The George W. Woodruff School of Mechanical Engineering, Georgia Institute of Technology, Atlanta, Georgia 30332, e-mail: mike.schatz@physics.gatech.edu; paul.neitzel@me.gatech.edu*

Key Words free-surface flow, surface-tension–driven instability, hydrodynamic instability, pattern formation, thermal convection, thermocapillarity, Bénard-Marangoni convection, liquid bridge, hydrothermal waves, oscillatory convection

■ **Abstract** This review summarizes recent experimental studies of instabilities in free-surface flows driven by thermocapillarity. Two broad classes are considered, depending upon whether the imposed temperature gradient is perpendicular (Marangoni-convection instability) or parallel (thermocapillary-convection instability) to the free surface. Both steady and time-dependent instabilites are reviewed in experiments employing both large- and small-aspect-ratio geometries of various symmetries.

1. INTRODUCTION

The interfacial (surface) tension σ characterizes macroscopically the molecular interactions that occur at the interface between two immiscible fluids. When the fluids are subjected to an externally imposed temperature difference ΔT, spatial gradients in σ may be induced with the largest values of σ typically occurring at the coldest regions on the interface ($\sigma_T \equiv -\frac{d\sigma}{dT} > 0$). Shear stresses at the interface arise to balance the surface-tension gradients, resulting in fluid motion; this is known as the Marangoni effect (Scriven & Sternling 1960). The flow penetrates into the bulk through viscous coupling to the motion at the interface; this is thermocapillary flow. (Similar surface-tension-driven flows can arise from gradients in other fields, e.g. concentration, electric field, etc; these cases are beyond the scope of this article.)

Thermocapillary flow arises in a wide range of problems of historical, fundamental, and practical importance. Bénard (1900) observed beautiful cellular flow patterns whose cause Rayleigh attributed to buoyancy. Much later, Pearson (1958) first provided the correct explanation in terms of the Marangoni effect. Bénard's work established thermal convection as a model system for exploring fundamental

questions in fluid mechanics, in nonequilibrium pattern formation, and in turbulence. Frequently, both thermocapillary and buoyancy effects are simultaneously present, and oftentimes thermocapillary convection is overshadowed by buoyancy-driven motion.

However, for small geometry and/or microgravity environments, this is not the case and thermocapillary is dominant. For example, thermocapillary driving of flow plays an important role in industrial applications including the growth of crystals in semiconductor materials, the rupture of thin films in heat transfer devices, the texturing of surfaces in magnetic storage devices, and the propagation of flames over liquid fuels.

Recent experimental work on instabilities in thermocapillary flow has focused on highly simplified cases in an effort to make close contact with theoretical studies. A liquid-gas two-fluid combination is usually chosen to provide a system that is simpler both to implement experimentally and to describe theoretically. Additionally, the liquid-gas systems are typically confined by boundaries with a high degree of symmetry. With these restrictions, it is useful to categorize the instabilities we describe into two general classes. In the first, known as Marangoni-convection instability (Section 2), the externally imposed ΔT yields imposed temperature gradients that are primarily perpendicular to the interface. Here, the basic state is static with a conduction temperature distribution; motion ensues with the onset of instability when ΔT exceeds some threshold. A second general class of thermocapillary flow is known as thermocapillary-convection instability (Section 3) whereby the externally imposed ΔT yields imposed temperature gradients that are primarily parallel to the interface. In these cases, motion occurs for any value of ΔT. For small enough temperature differences, the basic state is steady and considered theoretically to be either one- or two-dimensional. The instabilities of interest occur for larger ΔT and result in the appearance of either steady or unsteady three-dimensional flow. We focus here on the experimental description and refer the reader to Davis (1987) for a cogent theoretical description of the thermocapillary mechanisms at work in all cases we describe.

2. MARANGONI-CONVECTION INSTABILITY

2.1 Preliminaries

Thermocapillarity may drive flow when a liquid-gas system with an initially flat, horizontal interface is sufficiently heated from below and cooled from above (Figure 1). In this case, the strength of the thermocapillary driving is characterized by the Marangoni number $M = \sigma_T \Delta T d/\rho\nu\kappa$ in terms of liquid layer thickness d, temperature difference across the liquid layer ΔT, the liquid's density ρ, kinematic viscosity ν, thermal diffusivity κ, and surface tension temperature coefficient σ_T. With heating from below, buoyant effects are also typically present as characterized by the Rayleigh number $R = \alpha g \Delta T d^3/\nu\kappa$, with

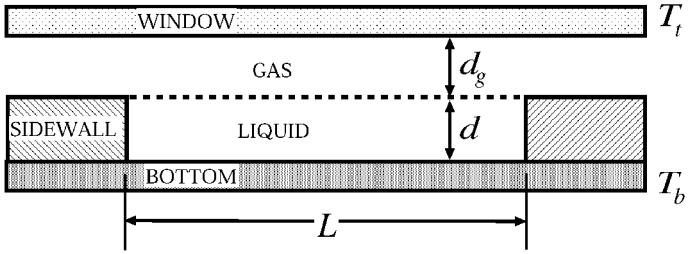

Figure 1 Cross section of apparatus for experiments on Marangoni instability. In most experiments, convection patterns are usually viewed from above and are bounded by sidewalls whose planform is circular.

the liquid's thermal expansion coefficient α, and the gravitational acceleration g. The ratio $M/R = \sigma_T/(\rho\alpha g d^2)$ characterizes the strength of thermocapillarity relative to buoyancy; the inverse $R/M \equiv Bo_D$ is called the dynamic Bond number. Flows driven solely by buoyancy ($M/R = 0$) are easily achieved in experiments by elimination of all free surfaces. (This simple case, known as Rayleigh-Bénard convection, is studied in the vast majority of experiments on thermal convection.) This review focuses on Marangoni convection (sometimes called surface-tension-driven Bénard convection or Bénard-Marangoni convection) where $M/R \geq 1$ provides a necessary condition (Section 2.2.1) for thermocapillarity to dominate over buoyancy. Thermocapillarity is most readily made dominant in experiments by choosing d sufficiently small; buoyant effects can be virtually eliminated by performing space experiments where g almost vanishes (Dupont et al 1992).

Experiments on Marangoni convection are most frequently performed with silicone oil-air layers. Choosing air as the upper fluid layer (Figure 1) simplifies the theoretical description by permitting the density and the viscosity of the upper layer to be neglected. Silicone oils (polydimethylsiloxanes) are chosen for the lower fluid layer because the oils have a very low surface tension. Silicone oil-air interfaces are virtually unsusceptible to surface-active agents (surfactants), which can dramatically alter the stability properties of Marangoni convection (Berg & Acrivos 1965). Moreover, silicone oils are readily available in a range of Prandtl number $Pr \equiv \nu/\kappa$ (typically $50 \lesssim Pr \lesssim 1000$). The polydispersity of commercial oils may affect flow dynamics; single component silicone oils of high purity can be obtained by simple distillation of commercial oils (Schatz & Howden 1995).

A judicious choice of experimental geometry can greatly simplify connecting the system's temperature field to heat transport across the layers. Typically, the bottom boundary temperature T_b is imposed uniformly by choosing the boundary's thermal conductivity to be much greater than that of the liquid layers. The temperature across the lower layer ΔT is defined by $\Delta T \equiv T_b - \langle T_i \rangle$, where T_i is the interface temperature and $\langle\rangle$ represents the spatial average horizontally

across the system. T_i can be obtained from noncontact optical measurements (Schatz et al 1999). In experiments where the air layer is unbounded above ($d_g \to \infty$; e.g. Bénard 1900, Cerisier et al 1987), heat transport is difficult to characterize because buoyancy-driven convection in the air layer will typically be present and can couple to thermocapillary flow in the oil layer in a way that can only be described with a full two-fluid model. The buoyant instability can be suppressed in the air layer by use of a top boundary of high thermal conductivity placed at a sufficiently small distance d_g above the interface; the top boundary is cooled uniformly at $T_t < T_b$ (Figure 1). In this case, heat transport in the air is dominated by conduction for a substantial range of M; this remains true even when forced convective motion in the air arises as the interface moves due to thermocapillarity (Eckert et al 1998). With this configuration, globally averaged heat transport can be obtained either from calorimetry measurements or from independent measurement of ΔT, T_b, and T_t (Pérez-García et al 1998). We use M defined in terms of ΔT to describe experiments with any value of d_g; however, a suitable alternative reference temperature $\Delta T_{cond} \equiv (T_b - T_t)Bi/(1 + Bi)$, with the Biot number $Bi = k_g d/kd_g$ (k and k_g are, respectively, the oil and air thermal conductivities), may be used for experiments where d_g is sufficiently small to prevent buoyant instability in the air layer. Although $\Delta T = \Delta T_{cond}$ only when heat is transported by pure conduction, ΔT_{cond} is still well defined above the onset of convection and is independent of the flow structure. (ΔT depends on the flow structure through $\langle T_i \rangle$.)

Lateral, thermal, and mechanical boundary conditions set by the sidewalls (Figure 1) can significantly affect Marangoni convection. Ideally, the temperature at the top of the sidewall should be equal to $\langle T_i \rangle$. However, this condition is practically never achieved, even for pure conduction, because it is difficult to match the thermal conductivity of the sidewall with that of the oil. Thus, lateral temperature gradients can result and induce thermocapillary convection near the sidewall (Section 3), which perturbs Marangoni convection. The mechanical attachment of the interface at the lateral boundary can also determine the strength of thermal perturbations to the flow. The liquid-gas interface should be flat, which typically requires pinning the contact line at an edge at the brim of a sidewall. Because the sidewalls are typically constructed from soft materials (e.g. acrylic, Teflon, nylon), whose thermal conductivity is close to that of silicone oil, some mechanical nonuniformity is usually present. The impact of the perturbations on Marangoni convection experiments can be ameliorated somewhat by measures such as buffer regions (Schatz et al 1995) or surrounding the sidewall on both sides with fluid (Ondarçuhu et al 1993a). Cases where the influence of sidewall perturbations may be important are discussed below.

2.2 Onset

Linear-stability analysis of the conduction (no fluid motion) state predicts one of two different primary instabilities may be observed in experiments when M

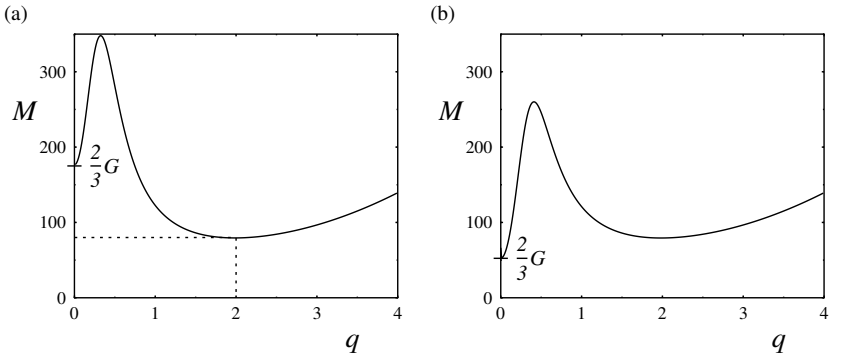

Figure 2 Marginal stability curves for Marangoni convection indicate two different types of primary instabilities can typically arise. The stability curves are computed for $\nu = 0.10$ cm^2 s^{-1} silicone oil under terrestrial gravity with $d \ll d_g$. (*a*) Short-wavelength modes ($q \neq 0$) are primary for thick oil layers; instability of these modes leads to the classic cellular flows studied by Bénard (1900). (*b*) For sufficiently thin oil layers ($d \leq 0.03$ cm), the global minimum is at $q = 0$, and modes with long-wavelength deformation of the interface become primary.

exceeds a critical value M_c that depends on the wavenumber q scaled on d (Figure 2). A short-wavelength ($q \approx 2$) primary instability arises when diffusion (thermal and viscous) is the main mechanism for damping perturbations at the interface (Figure 2*a*), whereas a different, long-wavelength ($q = 0$) primary instability arises when hydrostatic pressure is chiefly responsible for opposing perturbations (Figure 2*b*). Selection between short-wave and long-wave modes at onset is readily achieved in experiments since $M_c(q = 0)$ varies strongly with d: $M_c(q = 0) = 2G/3$ where $G \equiv 2gd^3/3\nu\kappa$ is the Galileo number.

2.2.1 Short-Wavelength Instability

Cellular patterns are found at convective onset due to short-wavelength instability; the morphology of the observed patterns depends on the aspect ratio L/d. The convection cells are typically hexagonal when L/d is large; by contrast, the cells' symmetry is strongly influenced by the shape of lateral boundary when L/d is small. Each of these cases is discussed in turn below.

2.2.1.1 Large Aspect Ratio Schatz et al (1995) examined both linear and nonlinear aspects of onset in Marangoni convection (Figure 3). Onset was observed at $M_c = 83.6$ with a precision of ± 0.5 but with an accuracy of ± 11 primarily due to the uncertainty in the thermal properties (k, κ, and σ_T) of the purified silicone oils used in the experiments. Comparison with linear theory requires accounting for the effects of both buoyancy, as determined by M/R and the spatial dependence of heat transport due to the normal-mode structure of interfacial temperature

Figure 3 Hysteresis at the onset of Marangoni convection. (*a*) Just prior to onset, weak convection perturbs the flow at the boundary for $\epsilon = -5.6 \times 10^{-3}$. (*b*) Finite amplitude convection with a nearly ideal hexagonal planform arises for $\epsilon = -2.3 \times 10^{-3}$. Upflow is indicated by dark regions. (*c*) The abrupt onset of Marangoni convection is exhibited by a plot of the Fourier mode amplitude A (from shadowgraph images) versus ϵ. Convection appears suddenly for slowing increasing ϵ (squares) and persists below onset for slowly decreasing ϵ (triangles).

perturbations. Spatially varying heat transport is described by a wavenumber-dependent Biot number $Bi_q(q) \equiv \frac{qk_g}{k \tanh(qd_g/d)}$, which is valid when pure conduction dominates heat transport in the air layer. The resulting linear theory for the experimental conditions of Figure 3 ($M/R = 40, Bi_q = 0.4$) predicts a somewhat larger value of $M_c = 95$ (Pérez-García et al 1998). [The comparison to linear theory described in Schatz et al (1995) characterizes heat transport using $Bi = 0.2$, which is valid only for $q \to 0$.] The linear onset is observed only indirectly because the instability is subcritical (i.e. akin to a first-order phase transition in equilibrium thermodynamic systems) (Figure 3*c*). A range of M exists where either conduction or convection is stable; in terms of $\epsilon \equiv \frac{M-M_c}{M_c}$, the range of bistability is found for $-0.032 < \epsilon < 0$. This hysteresis at onset is a nonlinear effect arising from the lack of up-down symmetry in the system (Cross & Hohenberg 1993). A variety of theoretical studies based on amplitude equations have predicted subcritical instability at onset (Scanlon & Segal 1967, Davis 1987, Bragard & Velarde 1998); the range of bicriticality predicted by the theories (0.2−2.2%) is smaller than the 3.2% indicated in Figure 3. As pointed out by Davis (1987), the predictions are only suggestive since the theoretical models are not rigorously self-consistent. Schatz et al (1995) noted that forcing at the lateral boundaries may obscure the observation of hysteresis at transition and could explain onset observed at very low values of M in earlier experimental studies of Marangoni convection (Koschmieder & Biggerstaff 1986).

Early experiments noted that the onset of cellular convection is accompanied by small but measurable deformation of the interface ($\sim$1 μm) where upflows (hot spots at the interface) may be concave (Bénard 1900) or convex (Jeffreys 1951). Linear theory accounts for this behavior by including both buoyancy and thermocapillary effects (Davis & Homsy 1980); concave upflows occur for thin, thermocapillary-dominated layers, while convex upflows occur for thicker, buoyancy-dominated layers. The experiments of Cerisier et al (1984) and accompanying stability analyses by Pérez-García et al (1985) found concave upflows

for $M/R \gtrsim 0.6$, which corresponds to $d \lesssim 0.3$ cm for silicone oil layers. This result suggests a necessary condition for experiments on Marangoni convection dominated by thermocapillarity.

Just above onset, Marangoni experiments exhibit highly ordered hexagonal patterns, whose wavenumber q changes as ϵ is increased. Schatz et al (1995) observed $q = 1.90$ at onset, while linear theory predicts a slightly larger $q_c = 1.97$ (Pérez-García et al 1998); linear theory and experiment cannot be rigorously compared due to the subcritical nature of the transition. As ϵ is slowly and monotonically increased above onset, Koschmieder & Switzer (1992) found the pattern wavenumber first increased and then decreased; they also found a larger range of ϵ with increasing q when the oil layer depth was decreased. Eckert et al (1998) confirmed these experimental findings and found a maximum $q(\epsilon)$ at $\epsilon \approx 1$ that was approximately 10% larger than q at onset. Numerical simulations with pure thermocapillary driving (no buoyancy) exhibit qualitatively similar ϵ dependence of q (Eckert et al 1998), which rules out an earlier suggestion by Koschmieder & Switzer (1992) that the maximum in $q(\epsilon)$ is caused by competition between thermocapillarity and buoyancy.

2.2.1.2 Small Aspect Ratio Koschmieder & Prahl (1990) investigated both the onset and the planform in Marangoni convection with aspect ratios L/d sufficiently small such that the lateral boundaries determine the flow structure (Figure 4).

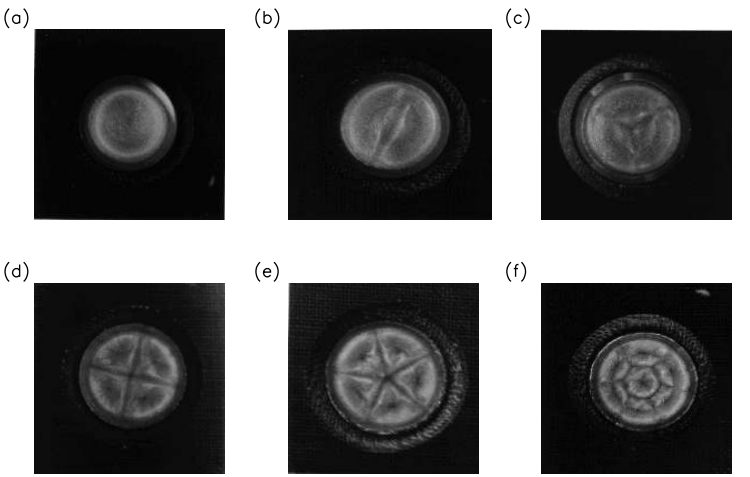

Figure 4 Small-aspect-ratio Marangoni convection with circular lateral boundaries from Koschmieder & Prahl (1990). (*a*) One-cell state: $M = 330$ and $L/d = 4.32$. (*b*) Two-cell state: $M = 81$ and $L/d = 5.31$. (*c*) Three-cell state: $M = 76.5$ and $L/d = 6.59$. (*d*) Four-cell state: $M = 78$ and $L/d = 6.79$. (*e*) Five-cell state: $M = 71$ and $L/d = 8.62$. (*f*) Six-cell state: $M = 74$ and $L/d = 8.96$.

At the smallest L/d with circular and square sidewalls, Koschmieder & Prahl (1990) found that convective flow exhibits the symmetry of the lateral boundaries with fluid upwelling in the center and flowing down near the sidewalls (Figure 4*a*). As L/d is increased for circular boundaries, patterns with discrete rotational symmetries are observed. Sector-shaped cells are divided by downflow boundaries that extend radially from the center of apparatus; the number of cells increases with increasing L/d (Figure 4*b–f*). For $L/d \geq 9$, a distinct group of boundary cells forms at sidewalls; these boundary cells encircle a group of polygonal interior cells, which can exhibit clear hexagonal symmetry. Koschmieder & Prahl (1990) observed a similar progression as L/d is increased for square boundaries; however, there is a greater tendency to observe nonsymmetrical patterns for $L/d < 9$. Ondarçuhu et al (1993a) observed similar nonsymmetrical patterns in experiments with an unbounded air layer and small L/d circular boundaries. Koschmieder & Prahl (1990) found that $M \approx 450$ at onset for their smallest $L/d = 1.9$. M at onset is observed to decrease rapidly with increasing L/d until attaining, for $L/d > 5$, a relatively constant value of $M \approx 60$; however, this onset value is well below the $M_c \approx 100$ predicted by linear stability theory (Pérez-García et al 1998). Quantitative small-aspect-ratio experiments are extremely challenging to perform because nonuniformities at the sidewalls, which are inevitably present in all Marangoni convection experiments (Section 2.1), become more important as L/d decreases. Thus, while theoretical studies can qualitatively capture some features such as the L/d dependence of M at onset (Davis 1987) and the appearance of some convective planforms above onset (Dauby & Lebon 1996), quantitative agreement between theory and experiment for onset in small-aspect-ratio experiments has not yet been achieved.

2.2.2 Long-Wavelength Instability

Deformation of the interface plays a central role in the onset and evolution of long-wavelength modes, in contrast to the short-wavelength modes where deformation is almost negligible (Section 2.2.1). The long-wave modes arise as the primary instability in terrestrial experiments with sufficiently thin silicone oil layers. These deformation modes should not be confused with a completely different long-wavelength instability that is predicted for a non-deformable, poorly conducting interface and an insulating bottom boundary (Pearson 1958). This instability has not yet been observed in experiments because the requisite boundary conditions cannot practically be achieved in experiments with thermally insulating liquids like silicone oils.

The observations of VanHook et al (1995, 1997) demonstrated that good predictions of onset by linear theory must include the effect of deformation on heat transfer. VanHook et al (1995) showed that linear theory overpredicts the onset of the instability by approximately 65% when the heat transfer through the interface is modeled by *Bi*. VanHook et al (1997) demonstrated that predictions are greatly improved by accounting for the increased (decreased) heat transfer where the air layer becomes thinner (thicker) as the interface deforms. When transport

is by pure conduction in the air layer, this effect is described by a two-layer Biot number $F = \frac{d/d_g - Bi}{1+Bi}$. In the experiments, F is typically varied by changing d/d_g, although F can also be modified by replacing the air layer with another gas of a substantially different thermal conductivity (e.g. helium). For large F (d/d_g large), theory predicts onset well, but for small F (small d/d_g), the theory significantly overpredicts onset. With $M/R > 100$ in the experiments, buoyancy effects are utterly negligible and cannot account for the discrepancies at onset. Experiments with the smallest values of F typically correspond to the smallest values of $d \lessapprox 100\ \mu$m where maintaining uniformity of the contact line at the sidewall is most difficult; therefore, experiments at the smallest F are typically subjected to substantial sidewall forcing (Section 2.1). Simulations by VanHook et al (1997) and Becerril et al (1998) show nonuniform boundary conditions at the sidewall advance the onset of instability and, therefore, can at least partially explain the discrepancies between theory and experiment.

VanHook et al (1995, 1997) showed experimentally that nonlinear evolution of long-wavelength flow states always leads to rupturing of the oil layer; steady convective states with small to moderate deformation have not been observed. The evolution toward rupture occurs in two different, mutually exclusive ways: either from a depression (Figure 5*a*) that evolves to form a hole in the layer where fluid drains away from a substantial area of the cell, or from an elevation (Figure 5*b*) that evolves to form a spike where the liquid rises up to a sufficient degree to make contact with the cooling window. VanHook et al (1997) demonstrated that weakly nonlinear analysis, a one-dimesional potential model valid in the strongly nonlinear regime, and numerical simulations (one- and two-dimensional) independently predict subcritical instability; rupturing is found in both the potential model and the numerical simulations. No stable deformed (unruptured) states were found in the experiments or analyses of VanHook et al (1997); however, more recently, Or et al (1999) predicted the existence of stable deformed states.

The evolution to either holes or spikes is captured by analyses and simulations that characterize heat transfer with F; in all cases, theory predicts that spikes form

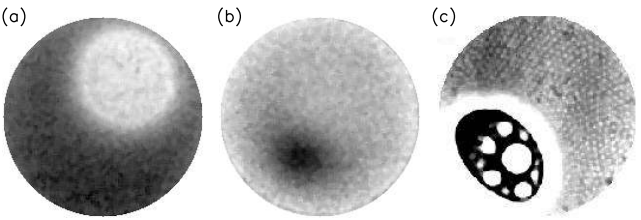

Figure 5 Infrared images of finite amplitude states arising from long-wavelength instability in Marangoni convection: (*a*) a localized depression (hole) is indicated by a light (warmer) circular region that occupies a substantial portion of the apparatus; (*b*) a localized elevation (spike) is indicated by a dark (cooler) circular region forming in the lower half of the apparatus; (*c*) coexistence of hexagons with a long-wavelength hole.

for $F \gtrapprox 1/2$ and holes form otherwise. (Models that describe heat transfer with *Bi* exhibit only the formation of holes.) The predictions are in good accord with the experimental observations where holes always form for $F < 0.48$, elevations form for $F > 0.58$, and either state may form for $0.48 < F < 0.58$. The largest values of F correspond to the smallest values of d_g; in this regime, the interface is most sensitive to the presence of the top boundary because a given deformation of the interface induces the largest relative variation in the air layer, favoring the formation of spikes. Smaller values of F correspond to larger d_g (for fixed conductivities of the gas and oil layers); the influence of the top boundary is reduced, favoring the formation of holes.

2.2.2.1 Competition with Short-Wavelength Modes Linear theory predicts a critical depth d_c where both the short- and the long-wavelength modes are simultaneously unstable (i.e. the two local minima in Figure 2 occur for the same value of M); long-wave modes are more unstable for $d < d_c$ and short-wave modes for $d > d_c$. By varying d in experiments with small F, VanHook et al (1995, 1997) only long-wavelength instability (holes) for $d < 0.017$ cm and short-wavelength hexagons for $d \geq 0.024$ cm, in good agreement with the linear stability prediction of $d_c = 0.023$ cm. In the range of $0.017 \text{ cm} \leq d < 0.024$ cm, the long-wavelength deformational mode arises first, in accord with linear theory, as ϵ is increased quasistatically with the liquid volume fixed; the growth of the long-wave mode forms a hole (here $F < 1/2$) and increases the local depth in the liquid layer surrounding the hole. As a result, the local value of M in the liquid surrounding the hole becomes sufficiently large to cause the formation of hexagons in the layer (Figure 5*c*). Thus, the long-wavelength mode can induce the short-wave instability. By contrast, the presence of the short-wave hexagons inhibits long-wavelength instability (Golovin et al 1997). For $d > d_c$, long-wavelength modes are never observed as a secondary instability of the hexagonal state. Furthermore, rapid ramping of ϵ leads to the formation of hexagons throughout the entire layer that inhibit long-wavelength modes even for fixed $d < d_c$. Hexagons can form first with fast ramping of ϵ since the time-scale of formation of the short-wave modes is the vertical diffusion time ($d^2/\kappa \approx 0.1$ s), while the time-scale for the long-wavelength mode is the horizontal diffusion time ($L^2/\kappa \approx 3$ hours–for a more precise estimate, see Wilson & Thess 1997). If ϵ is decreased slowly below the onset of hexagons, then the long-wavelength mode can form once the hexagons have disappeared.

2.3 Secondary Instability (Short-Wave Modes)

In large-aspect-ratio Marangoni convection, the hexagonal patterns observed at onset lose stability for ϵ sufficiently large. Two main scenarios have been identified experimentally where thermocapillarity is dominant. In experiments using silicone oils with very large $Pr \sim 1000$, hexagons become unstable to increasingly disordered polygonal patterns (Section 2.3.1) whereas in experiments with

smaller $Pr \sim 100$, hexagons lose stability to square patterns (Section 2.3.2). These different transition scenarios have been qualitatively identified in numerical simulations (Bestehorn 1996). Marangoni convection experiments have been conducted where buoyancy effects are dominant (Cerisier et al 1987a). Although such experiments are beyond the scope of this review, it is worth noting such systems exhibit secondary instabilities to roll patterns that are qualitatively similar to scenarios observed for Rayleigh-Bénard convection subjected to weak non-Boussinesq effects (Ciliberto et al 1990). No small-aspect-ratio experiments on secondary instabilities have been performed with $M/R \gtrsim 1$; the results of small-aspect-ratio Marangoni convection experiments with strong buoyancy effects are briefly discussed (see Section 2.3.3).

2.3.1 Large Aspect Ratio: $Pr \sim 1000$

Cerisier et al (1987b, 1996a, 1996b) demonstrated that defects govern the order-disorder transition observed in Marangoni convection experiments performed in this range of Pr (Figure 6). The dominant defect is a pentagon-heptagon pair (penta-hepta defect), which is equivalent to a dislocation in two of the three sets of rolls that superpose to form a hexagonal pattern (Cross & Hohenberg 1993). Measurement of the defect density ρ_d, the ratio of the number of nonhexagonal cells to the total number of cells, is a useful way to characterize the disorder; because penta-hepta defects are dominant, ρ_d is chiefly a measure of the relative number of pentagons and heptagons in the pattern (Cerisier et al 1996b).

Cerisier et al (1987b, 1996a) studied the evolution toward disorder as ϵ is increased. For low values of ϵ, patterns are dominated by hexagons; however, some fraction of defects are found even for small ϵ. Experiments with hexagonal sidewall

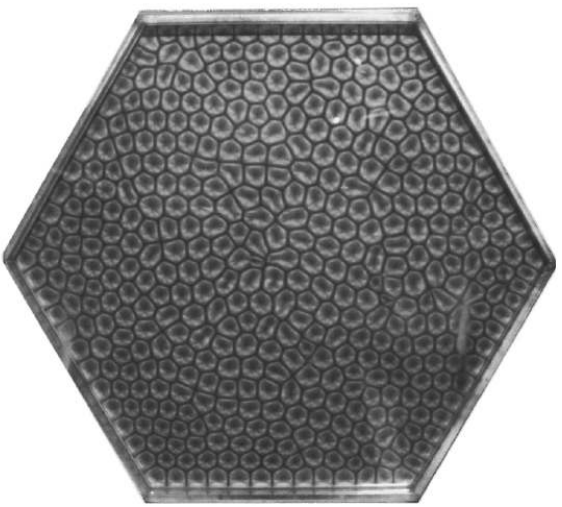

Figure 6 Disordered Marangoni convection at $Pr \sim 1000$ (from Cerisier et al (1996b).

boundaries exhibit $\rho_d \approx 0.04$ for $\epsilon = 0.05$; square and circular lateral boundaries exhibit somewhat larger values of ρ_d at the same ϵ. With increasing ϵ, ρ_d increases in a way that depends on Pr; ρ_d approaches 0.5 for sufficiently large ϵ. Cerisier et al (1987b) reported that $\rho_d(\epsilon)$ fluctuates even at small $\epsilon = 0.05$; this behavior is surprising given that hexagonal patterns at similar ϵ are stationary in experiments at lower Pr where time-dependent effects are expected to be stronger (Schatz et al 1999). Because, in at least some cases, the experiments of Cerisier are conducted with an unbounded air layer, buoyant instability in the air layer may be coupling to the flow and contributing to the pattern time dependence (Section 2.1).

Cerisier et al (1993, 1996a) also studied the evolution toward disorder at fixed ϵ by imposing regular patterns as initial conditions by means of an ingenious thermal technique. Experiments at fixed ϵ reveal that imposed patterns with different initial wavelengths evolve to a final mean wavelength that is unique. For most cases, the evolution toward the final mean wavelength involves the generation of defects that introduce increased disorder and a distribution of wavelengths about the mean in the pattern (Cerisier et al 1993). However, if the initial imposed wavelength of the hexagonal pattern is very near the final mean value, the final pattern exhibits substantially more order, even at large $\epsilon \approx 5$ (Cerisier et al 1996a).

In addition to measurement of ρ_d, more sophisticated approaches have been applied to characterize disorder. Methods such as radial and orientational correlation functions (Occelli et al 1983), disorder functions (Cerisier et al 1987a), and entropies (Cerisier et al 1996a) have some advantages; for example, disorder due to distortion of a hexagonal lattice can be characterized even in the absence of defects ($\rho_d = 0$). Statistical approaches that characterize topological properties [e.g. the average area for cells with n sides (downflow boundaries), moments of the distribution function for n] have been used (Cerisier et al 1996b). This approach permits comparison to a wide variety of other physical systems (soap froths, biological tissues, metallic structures, etc) where analogous disordered cellular patterns arise.

2.3.2 Large Aspect Ratio: $Pr \sim 100$

As ϵ is slowly increased, hexagonal patterns (Figure 3) lose stability to patterns of mixed symmetry (Figure 7*a*); with further increases in ϵ, the patterns evolve to nearly ideal square patterns (Figure 7*b*) (Nitschke & Thess 1995, Eckert et al 1998, Schatz et al 1999). This transition sequence arises via a local change in topology whereupon threefold vertices of the initial hexagonal cells become fourfold; an edge that separates two vertices shrinks to zero length, and the two vertices coalesce to form the intersection of four edges (Figure 7*c–f*). In hexagonal networks found in many physical systems, the four edges will swap neighbors as the intersection splits up into two new vertices that are separated by a new edge; this topological transformation is known as a T1 process (Cerisier et al 1996b). However, for the present case, this T1 process is arrested; as the vertices coalesce, the angle between adjacent edges changes from 120° to 90° and the intersection of four edges becomes stable. Initially, this process forms pentagons (Figure 7*e*).

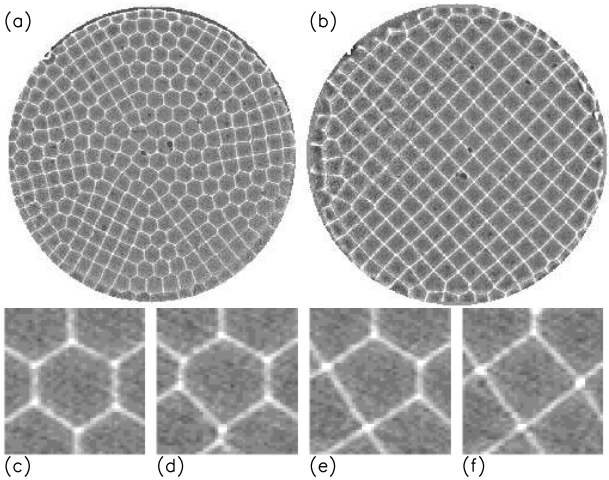

Figure 7 Transition to square patterns in Marangoni convection for $d = 0.072$ cm. (*a*) At $\epsilon = 3.9$, a stationary pattern of mixed hexagonal, pentagonal, and square symmetry is observed. (*b*) At $\epsilon = 7.23$, a stationary, nearly ideal square pattern arises. Close observation of a few cells demonstrates local changes in topology from threefold to fourfold vertices as ϵ is gradually increased from (*c*) 2.67, through (*d*) 2.98, and (*e*) 3.3, to (*f*) 3.89.

Moreover, the occurrence of this process induces formation of fourfold vertices in neighboring cells, leading to the appearance of chains of pentagons (penta-lines) in the pattern. With increasing ϵ, formation of additional fourfold vertices leads to the formation of squares, which dominate for ϵ sufficiently large (Figure 7*b*). As ϵ is then decreased, the square pattern loses stability; patterns of mixed symmetry as seen in Figure 7*a* reappear, and a planform dominated by hexagonal cells reappears with ϵ sufficiently small.

Both the wavenumber and the value of ϵ for the transition between hexagons and squares depend strongly on the previous history of the patterns. The relative fraction of square cells n_s is chosen as an order parameter to characterize the transition, which occurs at ϵ_s and corresponds to $n_s = 0.5$. If ϵ is increased until n_s just exceeds 0.5 (e.g., Figure 7*a*) and then is decreased, n_s exhibits hysteresis (Eckert et al 1998, Schatz et al 1999). The wave numbers exhibit little evidence of hysteresis in this range of ϵ. However, in experiments where ϵ is increased until obtaining a nearly perfect pattern of squares (e.g. Figure 7*b*), the observed hysteresis in n_s occurs at a larger value of ϵ_s. Furthermore, the transition at larger ϵ is accompanied by a substantial decrease in q. (Compare, for example, the wavenumber of square cells in Figure 7*a,b*.) The decrease in q persists as ϵ is cycled over a specified range. In other words, small q square patterns in turn induce small q hexagonal pattern when ϵ is reduced (Schatz et al 1999). Thus, the transition does not occur with unique values of ϵ_s or $q(\epsilon_s)$, although, in general, the wavenumbers for squares q_s and for hexagons q_h decrease with increasing ϵ. Numerical simulations by Eckert

et al (1998) exhibit a hysteretic transition that is dependent on Prandtl number P; they estimate the transition occurs at $\epsilon_{cond} = 0.28P^{0.68}$ where $\epsilon_{cond} \equiv \frac{M_{cond} - M_c}{M_c}$ (Section 2.1). This prediction lies above the range of experiments by Eckert et al (1998; $\epsilon_{cond} = 6.4$ predicted versus $3.5 < \epsilon_{cond} < 4.5$ observed) and in the range of experiments by Schatz et al (1999; $\epsilon_{cond} = 5.6$ predicted versus $4.5 < \epsilon_{cond} < 6.4$ observed); in the latter case, it should be noted that the simulations of Eckert et al and the experiments of Schatz et al differ in Bi, and the simulations do not include the dependence of the transition on pattern wavenumber observed in the experiments.

Eckert et al (1998) carried out careful heat-transfer measurements that demonstrate increased heat transfer associated with the appearance of square patterns (Figure 8). The heat transfer is characterized by the Nusselt number Nu, which is the ratio of heat flux measured experimentally to the heat flux that would arise solely from conduction for the same imposed T_b and T_t. The convective contribution to the heat transport, $Nu - 1$, exhibits a clear increase at values of ϵ that coincide with marked increases in n_s (Figure 8). This result suggests that square patterns rather than hexagons become more efficient at transporting heat for ϵ sufficiently large. Numerical simulations by Eckert et al (1998) exhibit similar behavior by showing that for small ϵ, hexagons are more efficient at heat transport than squares, but for ϵ sufficiently large, squares become more efficient. The comparison is qualitative, however, because the heat transport simulations are performed on only a single cell (hexagon or square); thus, for example, crossover occurs at much lower $\epsilon \approx 0.45$ than the observed hexagon-square transition in experiments.

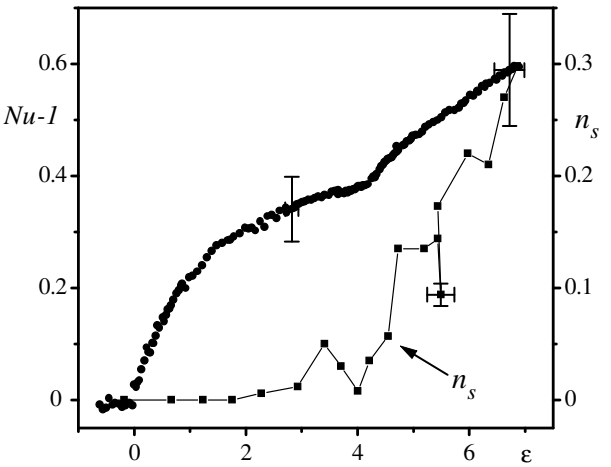

Figure 8 Measurements of convective heat transfer ($Nu - 1$) are compared with the relative fraction of squares n_s as a function of ϵ_{cond} at the onset of square instability for Marangoni convection (from Eckert et al 1998).

Experiments differ as to the temporal behavior of patterns at fixed ϵ. In the experiments of Eckert et al (1998), after hexagons lose stability, they exhibit patterns that continually evolve over slow timescales comparable to the horizontal diffusion time τ_h. By contrast, Schatz et al (1999) observed that all patterns (hexagonal, mixed, and square) are time independent for ϵ that has been fixed for a sufficiently long time ($\gtrsim \tau_h$). Simulations suggest that both square and mixed patterns are time independent for $P > 40$; however, the smaller aspect ratios investigated in the simulations can have a stabilizing effect on patterns that may not be present in the larger aspect ratio of the experiments. Future simulations at large aspect ratio should shed some light on this issue. Differences in buoyant effects may account for the different observations since buoyancy is stronger in the experiments of Eckert et al (1998). (The simulations neglect buoyancy.) As always with Marangoni experiments, nonuniformity at the lateral boundary can drive cell motion and may account for the time dependence in the experiments.

2.3.3 Small Aspect Ratio

No experiments have probed secondary instabilities in small-aspect-ratio systems where $M/R > 1$; however, Ondarçuhu et al (1993a,b, 1994) performed a series of experiments that studied the appearance of time-dependent flow in cases where both buoyancy and thermocapillarity are significant. As ϵ is increased, convection states that exhibit the symmetry of the container (Section 2.2.1) lose stability to time-independent states that break the symmetry. With further increases in ϵ, Ondarçuhu et al (1993a) found that the asymmetric states in square containers become time-dependent via a Hopf bifurcation and after increasing ϵ still further, an additional bifurcation occurs to symmetric oscillations. For convective flow in square containers, Ondarçuhu et al (1993b) demonstrated that the sequence of bifurcations was well-modeled by a Takens-Bogdanoff normal form. Studies of extensions of this model predict chaotic dynamics, which are observed in experiments (Ondarçuhu et al 1994).

2.4 Beyond Secondary Instability

Preliminary experiments indicate that square patterns lose stability to disordered time-dependent cellular flows when M is sufficiently large (Figure 9). Disorder and time dependence coincide as the preference for vertices with fourfold coordination number is lost; threefold vertices are most common but unstable, continually undergoing sideswapping T1 processes. With further increases in M, cell division (mitosis) is also observed. The average cell size is observed to increase monotonically with M, obtaining, for $M \sim 5000$, an average cell area nearly an order of magnitude larger than the cell area at the onset of convection. This coarsening is analogous to the growth of cell size in other cellular networks (e.g. soap films, magnetic bubbles), which exhibit power law scaling; preliminary experiments are

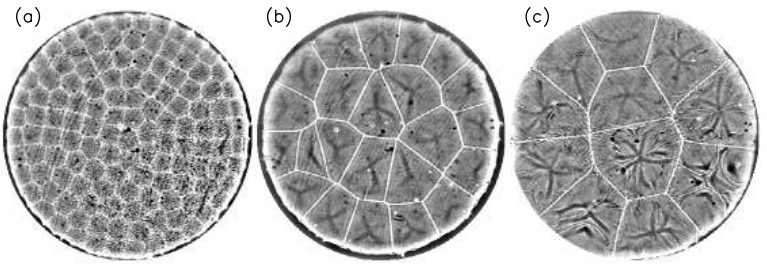

Figure 9 Observation of pattern coarsening in Marangoni convection as ϵ is increased beyond the onset of squares for $d = 0.122$ cm. The convection cells become become both larger and time dependent with increasing ϵ. (*a*) $\epsilon = 10.5$, (*b*) $\epsilon = 18.3$, and (*c*) $\epsilon = 47.8$.

suggestive of power law scaling in Marangoni convection. It should be noted that buoyancy effects are likely to be significant in this range of M.

3. THERMOCAPILLARY CONVECTION INSTABILITY

3.1 Preliminaries

Thermocapillary convection refers to motions driven by the application of a temperature gradient along the interface. Flow will be driven for any such surface-temperature gradient, no matter how small, and thus the existence of a critical, or threshold, temperature gradient is not required. These basic states become unstable for large enough applied temperature gradients and lead to alternate states consisting of either steady, cellular (most often, a form of roll cell) structures or oscillatory states.

Most of the research done over the last few decades on such instabilities has been motivated by the transition to oscillatory flow because of its importance in technological applications such as crystal growth. The appearance of oscillatory thermocapillary convection, coupled with solidification processes has been shown (see, e.g. the paper by Gatos 1982) to lead to a degradation of the resulting crystal. A review by Schwabe (1981) describes some of the earlier work on this problem.

For the purpose of classifying the types of experiments that have been performed, it is useful to think in terms of three categories, shown schematically in Figure 10. The direction of the body-force vector **g** is indicated for all three cases for those experiments conducted on Earth. The geometry of Figure 10*a* is a model of a float-zone or, for the case in which the temperature gradient is of a single sign along the free-surface, the half-zone. The latter case has been studied extensively as a model of the full float-zone. The actual crystal-growth application obviously possesses melting and solidifying interfaces at the top and bottom, but they will not be discussed here. The planar layer of Figure 10*b* is a model system motivated by the hydrodynamic-stability analysis of Smith & Davis (1983) (see also the

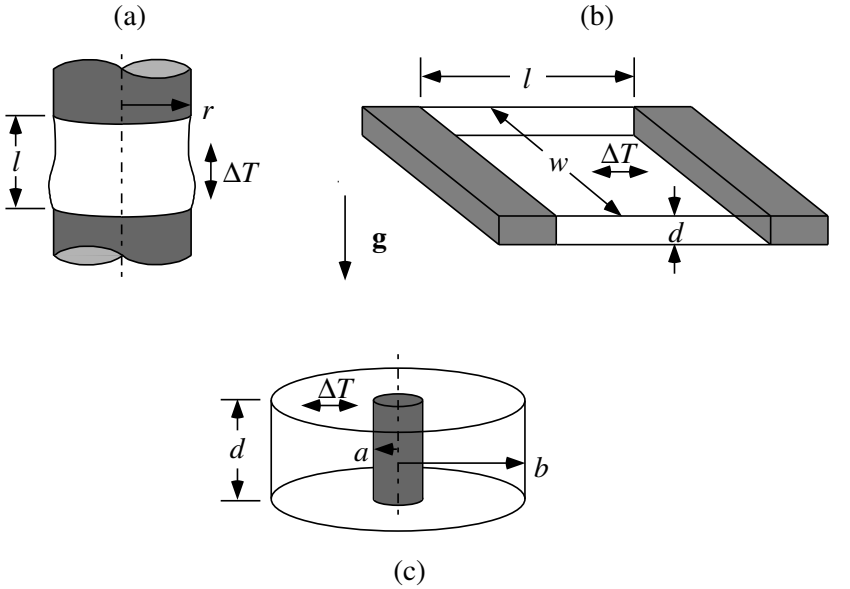

Figure 10 Types of thermocapillary convection: (*a*) liquid bridge, (*b*) rectangular layer or slot, (*c*) annular geometry.

review article by Davis 1987). These investigators discovered a new convective instability called a hydrothermal wave that was later shown by Xu & Davis (1984) to be relevant to the geometry of Figure 10*a* as well. For both cases (*a*) and (*b*), l is used to indicate the distance between solid walls in the direction of the applied temperature gradient. Finally, a limited number of experiments have examined the situation depicted in Figure 10*c*, for which the free surface is the upper, annular region $a < r < b$, where r (not shown in the figure) indicates the radial coordinate in a cylindrical coordinate system. Such a system could represent a model of the Czochralski crystal-growth process or be an alternate model for case (*b*), using the annulus to eliminate a sidewall effect. In case (*c*), the difference $b - a$ is analogous to the distance l in case (*b*).

As discussed for the systems of Section 2, silicone oils have been frequently employed as test liquids in the geometries of Figure 10. In addition to their resistance to contamination, these oils are transparent, permitting optical access to the interior of the flows, which has aided in the characterization of the instabilities. However, because of the motivation of crystal-growth processes and the fact that the Prandtl numbers of silicone oils and liquid metals differ by three or more orders of magnitude [$Pr = O(10^{-2})$ for molten silicon, while $Pr = O(10)$ or greater for silicone oils], these model systems are less than ideal for addressing the questions relevant to crystal growth. Nevertheless, much has been learned about the instability of thermocapillary convection from such studies, and the combination

of experiments, theoretical stability analyses, and numerical experimentation has been helpful in bridging the Prandtl-number gap.

3.2 Liquid-Bridge Instability

The vast majority of liquid-bridge investigations performed to date have focused on the so-called half-zone owing to its relevance to the float-zone process. Because this process had once been regarded as a candidate for space-based manufacturing of semiconductor material, some experiments have been performed aboard microgravity (μg) platforms such as sounding rockets or the Space Shuttle. The use of space was conceived, in part, because it was erroneously thought that oscillation-induced dopant striations were the result of the instability of buoyancy-driven convection. Experiments by Eyer et al (1985) demonstrated that material grown using the float-zone method in a μg environment produced crystal with dopant striations, thus confirming the suspicions that striations were caused by oscillatory thermocapillary, rather than buoyancy-driven, convection. The half-zone consists of a liquid bridge held between two solid, planar endwalls across which a temperature difference is applied. The usual case is to have the upper endwall hotter than the lower, contributing to a stabilizing axial buoyancy gradient. As such, the half-zone models the lower portion of an actual float-zone melt for which the hottest region of the free surface is somewhere between the melting and solidifying material interfaces. For all liquids of interest in the experiments described here, surface tension decreases with increasing temperature ($\sigma_T > 0$). Thus, the basic state of thermocapillary convection consists of a single toroidal roll, with the surface motion directed downward from the hot upper disk to the cold lower one. In spite of the relatively simple geometry of the half-zone, factors remain that complicate comparisons between experiments. One of these, the volume of liquid contained in the bridge, is discussed briefly below. However, even in situations for which the volume of liquid is chosen to be that of a right-circular cylinder of a diameter equal to that of the heaters, the interface deformation caused by Earth's gravity depends on the size of the zone and the physical properties of the liquid. Such shape changes influence the basic state and resulting stability properties.

Chun & Wuest (1979, 1982) and Chun (1980) employed 5 centistoke (cS) silicone oil, methanol, and octadecane half and full zones, using thermocouple data to determine the onset of oscillations. Often the thermocouple was inserted through the free surface, although this practice is recognized to be undesirable because of its intrusive nature. Chun & Wuest (1982) and Chun (1980) also examined the use of rotation of cold endwalls to counteract the effect of thermocapillarity through the centrifugal pumping of liquid with an opposite sense of circulation. Kamotani & Kim (1988) obtained similar results using rotation to stabilize 4 mm diameter half-zones of 2 and 5 cS silicone oil, although destabilization was observed for rotation rates in excess of 50 revolutions per minute.

Schwabe and colleagues have made substantial contributions to the literature. Preisser et al (1983) performed half-zone experiments with molten sodium nitrate

between graphite rods of $d = 4, 5$, or 6 mm. Although the Prandtl number was reported as having a value of 8.9, it actually appears to be closer to the value of 7. Using both flow visualization and temperature measurements (with thermocouples sometimes inserted through the free surface), they determined temperature differences, and hence, Marangoni numbers at the onset of oscillatory flow. They also determined azimuthal wavenumbers m, finding them to increase ($1 \leq m \leq 5$) as the aspect ratio $A = l/r$ is decreased from just less than 2.5 to 0.5; a correlation that appears to fit their data reasonably is $mA \approx 2.2$. Figure 11 shows sheet-illuminated flow-visualization photographs for oscillatory flow with azimuthal wavenumbers of $m = 1, 2$ for the upper and lower pairs, respectively. Subsequently, Velten et al (1991) conducted experiments with sodium nitrate, potassium chloride, ($Pr = 1$) and tetracosane ($C_{24}H_{50}$; $Pr = 49$), and additionally tested the configurations by reversing the sign of the surface-temperature gradient, as was also done earlier by Schwabe et al (1990). This work had reported that transition M values were higher in the heated-from-below cases (Schwabe et al 1990). Velten et al (1991) posited that the differences are due to alterations in the flows of gas surrounding the zone, which is confined by a larger quartz cylinder. In the heating from above case, this gas flow exhibits a pair of counter-rotating tori which, in turn, modify the radial heat transfer. Velten et al (1991) also reportedly observed

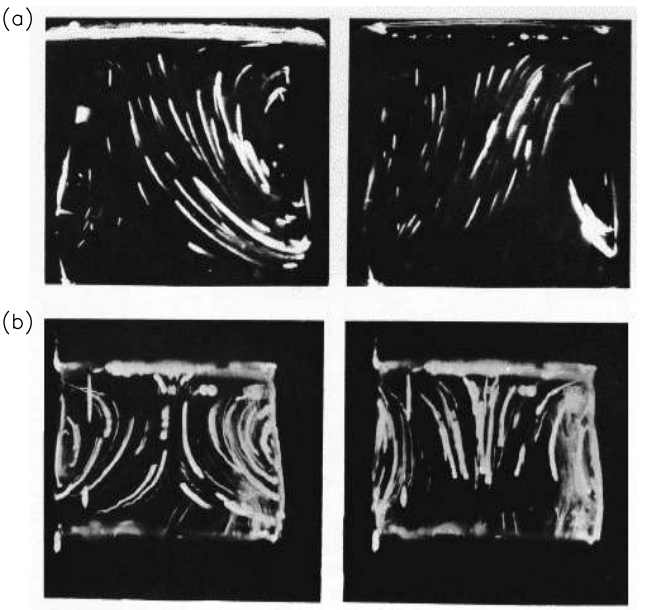

Figure 11 Oscillatory thermocapillary convection in a liquid bridge (Preisser et al 1983). The upper pair of photographs (*a*) show a non-axisymmetric $m = 1$ mode; the lower pair (*b*) show an $m = 2$ mode.

axisymmetric and other instabilities that appeared to be axially running waves, although not rotationally symmetric.

The experiments of Frank & Schwabe (1997) employed an upper solid surface consisting of sapphire to permit both uniform heating and visualization of the flow in the radial-azimuthal plane. Of particular interest was the measurement of various types of time-dependent flow: simple oscillatory flow, quasi-periodic, period doubling, and chaotic flows. Consequently, most experiments are performed at highly supercritical Marangoni numbers. Among the results obtained is the finding that earlier reports of axisymmetric ($m = 0$) oscillatory modes (e.g. by Velten et al 1991) were more likely misinterpreted $m = 1, 2$ pulsating modes.

Recently, Muehlner et al (1997) also performed experiments in a 2.6 cS silicone-oil ($Pr = 35$) bridge of unit aspect ratio, observing the surface-temperature distribution with an infrared (IR) camera and mirrors. They observed an $m = 1$ mode as the primary one at the onset of time dependence, with an $m = 2$ harmonic traveling with the same phase speed. At higher values of M, however, a secondary $m = 2$ mode traveling at the fundamental wave speed appears. Comparing these results with simultaneous measurements made with a thermistor placed near the surface showed that a misinterpretation of the thermistor data could allow the appearance of a subharmonic component to be mistaken for a period-doubling transition. The IR camera data suggest it actually arises from an interaction between the primary $m = 1$ and secondary $m = 2$ modes.

Finally, experiments by Petrov et al (1996, 1998) demonstrated suppression of oscillatory convection in liquid bridges through the sensing of surface-temperature variations and the application of surface heating using externally placed elements. Ideas from nonlinear dynamics were applied to effect control, with the control law constructed from observations of the bridge response to randomly applied perturbations. Attempts to effect control of a helical traveling-wave state using a single sensor/heater pair were unsuccessful—it changed the mode into a standing wave with a node at the sensor location. This was resolved with the addition of a second sensor/heater pair that permits the algorithm to distinguish between clockwise- and counterclockwise-propagating waves.

3.2.1 Microgravity Experiments

Experiments performed to date in a μg environment suffer, in general, from the limited time available for either a given experiment or for an ensemble of experiments. This, coupled with the limited availability of such environments, makes it very difficult to draw general conclusions from the results of this body of work. For example, Schwabe et al (1982) conducted sodium nitrate experiments in a 6 mm diameter half-zone of aspect ratio $A = 1.1$ aboard a sounding rocket with a 360 s μg period. For two supercritical states, the measured (thermocouple) frequencies for ground and μg experiments were virtually identical. On the other hand, measurements performed in microgravity and on ground by Schwabe & Scharmann (1985) showed instability at lower Ma for μg, with frequencies that were also slightly lower. The authors speculated that the

stabilizing buoyancy gradient present in the ground experiments could be partially responsible.

Yao et al (1997) used a 10-s drop tower to study changes in temperature and free-surface oscillations in half zones of 10 cS silicone oil ($Pr = 105$). The zones had 3 and 4 mm diameters with aspect ratios of $A = 1.6$. In addition, they were underfilled with $d/d_0 < 1$, where d is the minimum diameter of the zone and d_0 is the endwall diameter. Oscillation frequencies for highly supercritical states were observed to decrease in microgravity, and free-surface oscillation amplitude was observed to increase. Measurements of surface-wave patterns were also made, although the sample size was too small for general conclusions to be drawn. Some experiments were performed for states close to 1 g critical states.

Microgravity experiments were carried out aboard the Space Shuttle by Carotenuto et al (1998) using large (30–60 mm diameter) zones of 5 cS silicone oil ($Pr = 74$). Because of the time limitations of space experimentation and the desire to investigate as many conditions as possible, temperature ramping was used to increase ΔT through the transition to oscillatory flow. Velocities inside the zone and on the surface were measured using embedded tracer particles and either sheet illumination (interior) or a small laser diode mounted near the periphery of the zone, shining along the axis (surface). The latter was necessary due to the cylindrical-lens effect that obscures observations near the free surface. For the cases investigated, with $1.5 \leq A \leq 4$, the transition to oscillatory flow is seen as a standing wave [what Frank & Schwabe (1997) termed a pulsating mode] with azimuthal wavenumber $m = 1$. Based on their results and those of others, Carotenuto et al (1998) propose a scaling for the onset frequencies f as a function of aspect ratio of the form $\frac{f}{F} = \sqrt{\frac{l}{d}}$, where $F \equiv \frac{V_M M^{-1/3}}{2\pi\sqrt{ld}}$ is a reference frequency, $M = \frac{\sigma_T l \Delta T}{\rho \nu \kappa}$ the Marangoni number and $V_M \equiv \frac{\sigma_T \Delta T}{\rho \nu}$ is a Marangoni reference speed.

3.2.2 Liquid Metals

Only a limited number of experiments have been performed with liquid metals in spite of their relevance to the crystal-growth problem motivating this area of research. Part of the difficulty is the fact that such liquids are optically opaque, thus limiting diagnostic capabilities. Additional complications arise from the surrounding gaseous environment and/or chemical reactions between the melt and the material comprising the endwalls.

Jurisch (1990) used 4- and 6-mm diameter rods of Nb and Mo ($Pr = 0.025$) that were melted using an electron-beam heating facility. Surface temperatures were monitored with a micropyrometer and indicated the presence of oscillatory thermocapillary convection. Hysteresis was observed when power was increased/decreased, but the results are inconclusive, in part, because the zone length also changes with power input. Note that hysteresis is not observed in half-zone experiments using silicone oils.

Han et al (1996) created half-zones of mercury between two copper rods of 3 mm diameter. The use of inert materials such as graphite or stainless steel was not possible due to the fact that mercury does not wet them. In addition to the aspect ratio, the effect of zone shape was also of interest, here quantified in terms of V/V_0, the volume ratio of the zone to that of a right-circular cylinder of the same endwall diameter. The onset of oscillations was detected optically using interference fringes generated by light reflected from a laser onto a screen. The appearance of a surface skin that could suppress thermocapillary convection was noted by observing the motions of dust particles or other impurities on the free surface. Analysis of the mercury surface in cases when such a skin was observed to form indicated that it likely results from the presence of a copper-mercury amalgam that forms as the temperature difference between the copper rods is increased. Measurements of critical M were made for increasing and decreasing ΔT; the lowest value $M = 900$ is found for $A = 1.2$, $V/V_0 = 0.814$ with measurements made while M is increasing (the condition for which the skin is least likely to form).

Levenstam et al (1996) conducted experiments with molten silicon in a modified float-zone geometry, measuring oscillations with a thermocouple. They also performed companion three-dimensional, unsteady numerical simulations. From the latter, the first transition appears to be to a steady, three-dimensional mode, followed by the appearance of oscillatory convection.

3.2.3 Free-Surface Deformation

The experiments of Yao et al (1997) and Han et al (1996) reported on above included considerations of the volume of liquid occupying the liquid bridge. Other sets of experiments by Hu and colleagues (Cao et al 1992; Shu et al 1994) have also examined the influence of free-surface deformation as quantified by either a diameter ratio or volume ratio. More systematic treatments of this effect have been given by Monti et al (1992) and Hu et al (1994); the former experiments have been extended by Sumner et al (2001). An interesting feature of these results is the existence near $V/V_0 \approx 1$ of a local maximum in the value of M at which oscillations appear. Neither numerical experimentation (Shevtsova & Legros 1998) nor energy-stability theory (Sumner et al 2001) has yet succeeded in fully explaining the presence of this maximum.

3.3 Planar Rectangular Layers and Slots

These geometries (Figure 10*b*) are characterized by rectangular horizontal cross-sections. In the slot geometry, the planform aspect ratio $l/w \ll 1$, making these flows resemble thermocapillary-flow analogs of the driven-cavity problem. The experiments that have been performed in layers with $l/w = O(1)$ have been motivated by the theoretical analysis of Smith & Davis (1983), which predicts a direct transition from a steady, unicellular basic state to an oscillatory state in the form of hydrothermal waves.

3.3.1 Slot Experiments

Daviaud & Vince (1993) examined thermocapillary convection in a slot of $l = 1$ cm stream-wise and $w = 20$ cm span-wise extents using 0.65 cS silicone oil ($Pr = 10$). A temperature difference is imposed through copper endwalls, and shadowgraphic visualization is done through the transparent glass bottom of the apparatus. As in later experiments by others, a meniscus exists at all vertical surfaces, meaning that the free surface is not flat. When critical temperature differences are exceeded, patterns of longitudinal (i.e. in the stream-wise direction parallel to the imposed temperature difference) waves appear. For small layer depths ($d < 2.8$ mm) these patterns propagate nearly laterally, while for the larger depths examined (up to 10 mm) stationary rolls are observed. The depth $d = 2.8$ mm at which this change occurs corresponds to the condition $Bo_D = 1$, where Bo_D is the dynamic Bond number (Section 2.1). This transition point is indicative of a change in the dominant flow driver from thermocapillarity (thin layers) to buoyancy (thicker layers). The authors tried unsuccessfully to compare their results with the theory of Smith & Davis (1983); for large layer depths the comparison is clearly unwarranted because of geometrical considerations, but for small depths (e.g. $d = 0.8$ mm) significant differences exist between the critical Marangoni number and frequencies obtained from theory and experiment. These may possibly be related to the small stream-wise extent of the container used.

Gillon & Homsy (1996) were concerned with transitions from two- to three-dimensional flow rather than with the onset of time dependence. Their experiments were performed using 0.65 cS silicone oil ($Pr = 8.4$ at 25°C; $Pr = 9.5$ at 13°C) in an apparatus (with glass endwalls) with stream-wise aspect ratio $l/d = 1$ and a span-wise aspect ratio $w/d = 3.8$. Particle-image velocimetry was utilized to determine velocities at various span-wise locations. The cavity was underfilled with liquid to a depth of 0.68 of the height of the endwall. The contact angle was estimated to be 53° (whether the contact line was pinned at the endwall top was not stated, although this is indicated in their figure). The range of Marangoni numbers investigated was $6.33 \times 10^3 \leq M \leq 4.22 \times 10^5$ corresponding to temperature differences $0.3°\text{C} \leq \Delta T \leq 20.0°\text{C}$. The flow was determined to be two-dimensional, with no span-wise variation for $M < 1.1 \times 10^5$. Transitions to three-dimensional flow were determined by integration of the stream-wise velocity profile (fitted with splines) over the depth of the layer because values differing from zero are indicative of mass flux in the spanwise direction. The three-dimensional effects were observed to begin at the spanwise sidewalls and propagate inward, characteristic of an imperfect bifurcation; no evidence of hysteresis was observed, indicating the bifurcation to be supercritical. The best estimate for the transition to three-dimensional flow (obtained from visualization) is $M = 1.5 \times 10^5$. Spanwise visualization through the plane midway between the heated/cooled endwalls indicates the structure to be cardioid and approximately cubical, in agreement with numerical simulations of Mundrane & Zebib (1993), which were performed

assuming a 90° contact angle. Gillon & Homsy conclude that the instability is therefore "associated with the thermocapillary vortex, as modified by the buoyancy layers on the side walls, and is unassociated with free surface deflections and is insensitive to the curvature of the meniscus."

Finally, Braunsfurth & Homsy (1997) conducted experiments (using acetone with $Pr = 4.44$) that are similar to those of Gillon & Homsy (1996) but with the additional feature that both horizontal aspect ratios are held fixed at the same value and oscillatory flow is also observed. That is, the container has a (nearly) square footprint and depth is varied. No attempt is made to pin the contact line to form a flat surface. Particle-image velocimetry is used to obtain quantitative velocity data and to determine the onset of three-dimensional flow in the form of longitudinal (stream-wise) rolls. The transition curve for the onset of three-dimensional flow was determined to be $M_c = 10^6 - 2.7 \times 10^5 A$, where $A = l/d = w/d$ is either of the horizontal aspect ratios. The reason for the decrease in the transition Marangoni number with increasing aspect ratio is attributed to the fact that the sidewalls play less of a constraining role for larger A (although the authors properly caution that all parameters are changing when A is changed). The onset of three-dimensional flow is also observed to result in the flow at the free surface at the centerline location along the cold wall moving in the direction opposite to that which would be expected from either buoyancy or thermocapillary considerations. The transition to oscillatory flow is marked by the growth of this backward eddy filling as much as half the container (see Figure 12*a*) and the appearance of a small eddy at the hot wall, which ultimately oscillates in both size and strength (Figure 12*b*). For $A < 3.5$ and $A > 5$, oscillations are regular with frequencies of roughly 0.7 Hz; for A near 4.5, however, long, transient periods are observed prior to the establishment of a regular oscillation. The authors speculate on an instability mechanism for the onset of oscillatory flow related to the existence of a meniscus and the backward eddy coming from the hot wall, which moves the free-surface stagnation point toward the cold wall, thus strengthening the thermocapillary eddy.

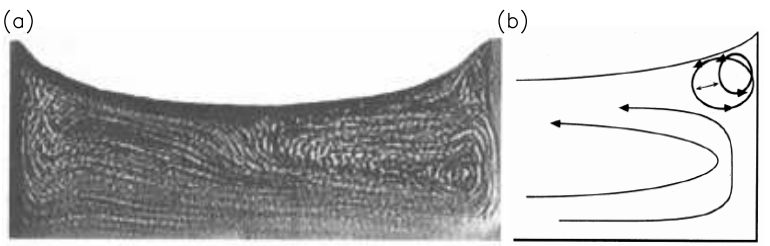

Figure 12 Oscillatory thermocapillary-buoyancy flow in a cavity from Braunsfurth & Homsy (1997): (*a*) streak visualization, (*b*) schematic diagram of oscillating corner eddy in (*a*).

3.3.2 Planar Rectangular Layers

This class of experiments is designed to most closely mimic the conditions of the Smith & Davis (1983) analysis, which assumes a layer of infinite horizontal extent, but with a return-flow basic state, i.e. including pressure-driven flow along the bottom of the cavity as required to satisfy continuity in a cavity of finite extent. Typically, for these experiments, both horizontal dimensions are large in comparison with the depth of liquid layers being considered, but this is not universally true. Villers & Platten (1992) performed both numerical and laboratory experiments to examine thermocapillary convection in a laterally heated layer. Their numerical simulations were two-dimensional and compare well with measurements for cases of steady unicellular and multicellular convection. Experiments were performed in an apparatus with $l = 30$ mm, $w = 10$ mm, and a conducting bottom using acetone ($Pr = 4.24$ at 20°C). No attempt was made to pin the contact line, which resulted in the presence of a meniscus. Quantitative flow measurements were performed using laser-Doppler velocimetry (LDV), which is adequate for basic-state characterization but not well suited to time-dependent situations. In particular, it is difficult with point measurements to sort out the spatial structure of the unsteady flows. Villers & Platten (1992) always observed a first transition from steady unicellular flow to steady multicellular flow. This transition was also observed in the later experiments of Riley & Neitzel (1998) (who used a liquid of slightly larger Prandtl number $Pr = 13.9$), but only for layers whose depths corresponded to $Bo_D > 0.2$. A calculation of dynamic Bond numbers from the tabulated data of Villers & Platten (1992) shows them to be quite large; in fact, only one experiment was conducted at $Bo_D < 0.2$. The numerical simulations for time-dependent flow performed by Villers & Platten should not be expected to yield results in good agreement with their unsteady experiments since they were two-dimensional and the anticipated instability is clearly three-dimensional.

Subsequently, De Saedeleer et al (1996) conducted experiments using decane ($Pr = 15$) in an apparatus of 10 mm span-wise width w but variable stream-wise length l. Like Villers & Platten (1992), they employed LDV to measure velocity profiles and detect transitions. Once again, no attempt was made to pin the contact line. These investigators realized, however, the importance of measuring the actual temperature gradient in the liquid for the purpose of computing the Marangoni number due to the presence of surface thermal boundary layers at the heated/cooled walls. These measurements were made by inserting a small thermocouple just beneath the surface, alternating between hot and cold endwalls (moving with a step size of 1 mm). Like Villers & Platten (1992), they found the first transition to be to a steady, multicellular state with transitions to oscillatory flow occurring at larger Marangoni number. For two of the cases described (with layer depths of 2.5 and 3.6 mm), calculations of the dynamic Bond numbers yield values of 0.51 and 1.05, respectively, which are well above the maximum value reported by Riley & Neitzel (1998) for the appearance of pure hydrothermal waves.

Riley & Neitzel (1998) were the first to experimentally verify the direct transition from steady, unicellular thermocapillary convection to an oscillatory, hydrothermal-wave state. Their experiments were performed in a variable-depth layer of rectangular cross-section ($l = 30$ mm $\times$ $w = 50$ mm) using 1 cS silicone oil with $Pr = 13.9$ as the test liquid. In order to obtain layers of uniform depth, variations attributed to the presence of a meniscus were eliminated by having the free surface pinned at a sharp edge, the top of which was coated with a wetting barrier. By adjusting the position of a vertically movable (insulating) bottom and the liquid volume, a flat interface was attained. Transitions between various states were determined through a combination of sheet-illuminated flow visualization, shadowgraphy (which is sensitive to the onset of time dependence), and IR thermography of the free surface. It was found that, when thick layers (i.e. $d \gtrsim 1.2$ mm in this apparatus) were employed, the observed transitions were from steady, unicellular flow to steady, multicellular flow, as observed by Villers & Platten (1992) and De Saedeleer et al (1996), prior to the onset of time-dependent flow. However, for thinner layers, the hydrothermal-wave transition predicted by Smith & Davis (1983) was observed. Figure 13 shows thermographs of the free surface for the hydrothermal-wave, steady-multicell and oscillatory-multicell states. The transition map determined for this set of experiments is provided in Figure 14. The Smith & Davis (1983) theory was developed assuming zero body force, which implied a dynamic Bond number of zero. Because Bo_D contains the square of the layer depth in its numerator, thinner layers begin to approximate the theoretically assumed state. The transition points appear to converge well to a zero-Bond-number linear-stability limit (marked by an $\times$ on the ordinate of Figure 14)

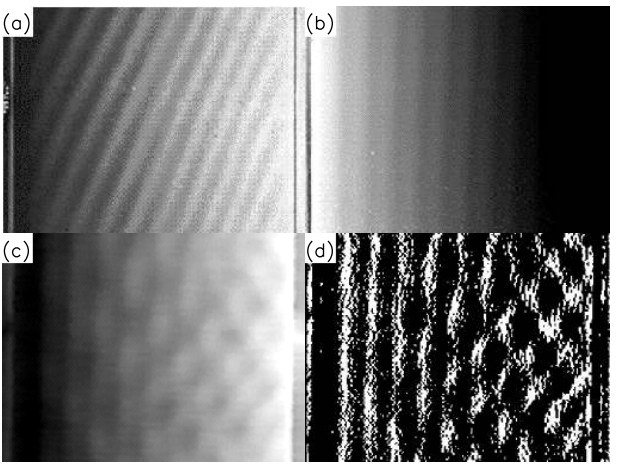

Figure 13 Thermocapillary flow states in a rectangular layer: (*a*) hydrothermal waves (HTW), (*b*) steady multicellular flow (SMC), (*c*) oscillatory multicellular flow (OMC), (*d*) enhancement of (*c*).

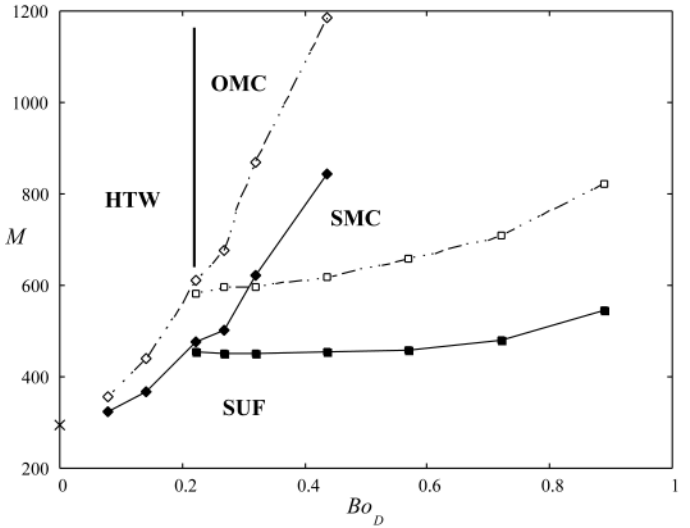

Figure 14 Phase diagram of thermocapillary flow states in a rectangular layer. SUF refers to steady unicellular flow, although there is always the presence of an eddy near the hot wall. Solid symbols are for M computed using $\partial T/\partial x$, the actual gradient, in the core flow; open symbols are for M computed using $\Delta T/l$, the overall gradient.

appropriate for $Pr = 13.9$. The value of the dynamic Bond number below which pure hydrothermal waves were observed is roughly $Bo_D = 0.2$. As observed by De Saedeleer et al (1996), to obtain the best comparisons with theoretical results these investigators found it necessary to determine the actual temperature gradient in the core of the flow, away from the thermal boundary layers near the heated and cooled boundaries. In the case of these experiments, this was done nonintrusively using the overhead IR thermographs.

Benz et al (1998) demonstrated that the hydrothermal-wave state found by Riley & Neitzel (1998) could be suppressed by interfering with the instability mechanism postulated by Smith & Davis (1983) and Smith (1986). Since, for high-Pr liquids, this mechanism involves a communication between free-surface temperature perturbations and bulk-liquid temperature, Benz et al (1998) speculated that by eliminating the free-surface temperature oscillations caused by hydrothermal waves this coupling could be broken and the oscillations would cease. This scheme was demonstrated using the same apparatus as employed by Riley & Neitzel (1998). Free-surface temperature oscillations of a hydrothermal-wave state were sensed at two locations using an infrared camera, allowing the phase speed of each wave to be determined. At a location further downstream (in the sense of the wave-propagation direction), a CO_2 laser used the actual temperature signature of each hydrothermal wave to supply heat to troughs of disturbance temperature. When done successfully, hydrothermal waves disappeared downstream of the periodic-heating location. Suppression of waves through the

application of constant surface heating was also demonstrated, although it was pointed out that this merely effected a change of the basic state rather than control of the instability.

3.4 Planar Layers in Cylindrical Geometries

For the final category of thermocapillary-convection instabilities, we examine the cylindrical geometry of Figure 10*c*. As described in the preliminary remarks, this geometry might be used to model the Czochralski crystal-growth process in which a crystal is pulled from a crucible of molten material. Were this the case, then the outer portion of the annulus would be heated and the inner portion (simulating the crystal) cooled. Temperature gradients in the deep-liquid cases described below are reversed so that none represents such a model. When convection is considered in very thin layers, one may be approximating the flows discussed in Section 3.3.2, but without the effect of sidewalls. Consider the case in which the inner portion of the annulus is heated and the outer cooled so that the basic state of unicellular motion consists of a flattened torus with motion outward along the free surface. In order for the results from experiments conducted in such a geometry to be comparable with, for instance, those of De Saedeleer et al (1996), Riley & Neitzel (1998), or the theory of Smith & Davis (1983), the effect of curvature would have to be minimized, which implies that $a/b \to 1$, akin to the small-gap assumption often made when discussing the stability of Taylor-Couette flow (DiPrima & Swinney 1981). In addition, approximation of the assumption that $l/d = (b-a)/d \to \infty$ requires the fabrication of a large apparatus. For instance, if one were operating with a nominal depth of 1 mm and $l = 30$ mm as in the experiments of Riley & Neitzel (1998), attainment of a radius ratio $a/b = 0.95$ would require an apparatus with an outer-wall radius of 600 mm. None of the experiments described in the following meets such requirements.

3.4.1 Thin Layers

A pair of papers describe experiments conducted in shallow, annular regions. Schwabe et al (1992) performed experiments in both annular ($a = 20$ mm and $b = 77$ mm, so that $a/b = 0.26$) and rectangular geometries (although the bulk of the presented results were for the former case) using ethanol ($Pr = 17$). A cold, copper bottom was used for the annulus, whereas both this and an insulating bottom were used for the rectangular geometry. In the annulus, the meniscus was eliminated at the inner hot boundary, but no attempt was made to eliminate it at the outer cold boundary, in spite of statements regarding the necessity of obtaining a flat interface. In all instances, the observed transitions were from a single-cell to a multicell state prior to the onset of oscillatory flow. It was suspected that this transition was due to the bottom boundary condition in the annulus, but experiments with an insulated boundary in the rectangular geometry yielded similar results. A rough computation of the dynamic Bond numbers appropriate for the experimental cases considered yielded values roughly an order of magnitude larger than those

determined by Riley & Neitzel (1998) to be the maximum at which hydrothermal waves could be observed. Oscillatory convection of two types was observed in the annulus: short-wavelength instabilities, which propagated obliquely, and long-wavelength instabilities, which propagated radially near onset (radial symmetry was broken at higher M). Short-wavelength instabilities were preferred for depths less than 1.4 mm and long waves for depths greater than this, although both were observed over the entire range of depths investigated. Surface deformations were observed with the aid of a shadowgraphic technique and are an order of magnitude higher for the long waves than for the short ones. Finally, the authors recognized the importance of computing M based upon the actual surface-temperature gradient. When doing so, transition values of M were computed that are more in line with the theoretical predictions of Smith & Davis (1983) for rectangular layers, although the geometries differ.

Ezersky et al (1993) performed experiments using 5 cS silicone oil in an annular geometry of 100 mm diameter for which heating is supplied using a copper cylinder mounted flush with the bottom of the liquid layer. Consequently, the surface-temperature gradient is created through indirect heating of the free surface by the natural convection (driven by either/both vertical and horizontal temperature gradients) of hot liquid near the heater. The diameter of the heating cylinder is not stated in the paper, but from the sketch, the aspect ratio appears to be roughly the same as that used by Schwabe et al (1992), although the basic state is different. Observations of unstable flows are made using shadowgraphic imaging of the free surface, detecting the presence of flow-induced surface waves. For $d < 0.3$ cm the first transition is to a state of concentric, steady rolls. For larger depths, such rolls were not observed; rather, the steady convection transforms to a traveling-wave state. At large temperature differences, numerous thermal plumes were observed in the heated region that gave rise to waves propagating away from this region. For smaller temperature differences, the plumes were absent. While these investigators believe they have observed pure hydrothermal waves, the later work of Riley & Neitzel (1998) suggests that this is likely not true. Finally, Ezersky et al (1993) discussed theoretically determined critical Marangoni numbers and frequencies for their experiment in spite of the fact that their basic state has never been subjected to an analysis that would have determined these values.

3.4.2 Deep Layers

Two teams of investigators have experimented with the deep-annulus configuration. Here, of course, the basic state is entirely different from that just described because the thermocapillary-driven eddy does not normally extend to the bottom of the vessel. Kamotani et al (1992) presented results of terrestrial laboratory experiments (subsequent microgravity experiments were also performed) in a deep-annular geometry in which the surface-temperature gradient is imposed by heating a wire (cylinder) located at the origin and cooling the outer cylinder. Results are presented in terms of an S parameter defined as $S \equiv \frac{\sigma_T \Delta T}{\sigma Pr}$, which is meant

to account for surface deflection. Thermocouples are used for point temperature measurements, and infrared thermography is employed to sense the free-surface temperatures. The appearance of oscillations is marked by a wavy return-flow pattern which precesses azimuthally. As the aspect ratio becomes large ($d/b \rightarrow 2$), the critical value of the S parameter at which oscillations appear approaches $S = 0.007$, four times larger than that found in a float-zone experiment, which, according to the authors, "suggests that the critical value of S is a function of configuration."

Lavalley et al (2001) performed numerical simulations and conducted experiments in a deep-annular region similar to that studied by Kamotani et al (1992). The test liquid was 1 cS silicone oil and two test cells were employed, one designed to permit flow visualization and particle-image velocimetry without extensive correction to compensate for index-of-refraction effects. Attempts were made to achieve a flat surface in one of these cells through the establishment of pinned contact lines. Results indicated that the presence of a meniscus served to increase the value of the Marangoni number at which oscillations were observed, a feature of likely relevance to some of the other experiments discussed above. Agreement between the numerical simulations, performed assuming a flat, nondeformable interface, and experiments is quite good, both qualitatively and quantitatively. As a result, Lavalley et al (2001) conclude that free-surface deformation due to disturbances plays no role in the instability. Finally, the character of the instability appears to be purely hydrodynamic and not of the hydrothermal-wave variety appropriate to half zones of liquids of similar Prandtl number.

4. FUTURE DIRECTIONS

Future experiments on control of thermocapillary instabilities could have broad fundamental and practical impact. The inherent two-dimensionality of interfacial driving suggests that direct measurement and manipulation of surface-tension gradients is feasible for a wide range of M in some thermocapillary flow problems. Benz et al (1998) demonstrated that optical methods can be used to both probe and alter thermocapillary flow. Further development of optical techniques should permit nearly simultaneous operation at multiple independent locations in the flow. Experiments with such multipoint capabilities would provide valuable test beds for advancing understanding of the behavior of spatially extended flows and could suggest ways to control dynamics that are complex in both space and time (e.g. spatiotemporal chaos).

Thermocapillarity may prove useful for the management of micron-sized droplets in fluidic devices constructed using microelectronic fabrication technologies. Planned applications such as genetic analysis and chemical sensing in these devices require precise metering of picoliter fluid volumes. Surface forces like thermocapillarity are important at this scale; thermocapillary instabilities that lead to rupturing

(Section 2.2.2) might be employed to subdivide tiny droplets into volumes of any desired size.

One recently explored phenomenon that may be driven by thermocapillary flow is the forced noncoalescence of two bodies of the same liquid. If the bodies are at sufficiently different temperatures, thermocapillary-driven free-surface motion will drag a layer of surrounding fluid into the gap between the free surfaces, thereby keeping them apart [see Dell'Aversana & Neitzel (1998) for a general overview]. Under certain conditions, however, Dell'Aversana et al (1997) showed that the associated flows become unstable and exhibit oscillatory flow that may be undesirable in some applications. Such instabilities need to be better understood if these applications are to be pursued.

As pointed out above, the crystal-growth applications that motivated extensive research on unstable thermocapillary flows involve molten liquids of extremely low Prandtl number. These low-Prandtl-number cases have received little attention from experimentalists because of the hostile nature of the environment (e.g. very high temperatures) and the opacity of liquid metals to visible light. Recent work by Hibiya and his collaborators (Hibiya et al 1998, Nakamura et al 1999) has employed X-ray interrogation of flow fields in molten silicon with embedded tracer particles, and Koster and colleagues (Pool & Koster 1994; Campbell & Koster 1994, 1997) have also used radiography to track melting/solidification fronts in crystal-growth melts. Such techniques offer promise for additional quantitative data to further the understanding of instabilities in such systems.

ACKNOWLEDGMENTS

This work was supported by the Microgravity Research Division of NASA (GPN) and the National Science Foundation (MFS). MFS is a Cottrell Scholar of the Research Corporation.

LITERATURE CITED

Becerril R, VanHook SJ, Swift JB. 1998. The influence of interface profile on the onset of long-wavelength Marangoni convection. *Phys. Fluids* 10:3230–32

Bénard H. 1900. Les tourbillons cellulaires dans une nappe liquide. *Rev. Gén. Sci. Pure Appl.* 11:1261–71, 1309–28

Benz S, Hintz P, Riley RJ, Neitzel GP. 1998. Instability of thermocapillary-buoyancy convection in shallow layers. Part 2. Suppression of hydrothermal waves. *J. Fluid Mech.* 359:165–80

Berg JC, Acrivos A. 1965. The effect of surface active agents on convection cells induced by surface tension. *Chem. Eng. Sci.* 20:737–45

Bestehorn M. 1996. Square patterns in Bénard-Marangoni convection. *Phys. Rev. Lett.* 76:46–49

Bragard J, Velarde MG. 1998. Bénard-Marangoni convection: planforms and related theoretical predictions. *J. Fluid Mech.* 368:165–94

Braunsfurth MG, Homsy GM. 1997. Combined thermocapillary-buoyancy convection in a

cavity. Part II. An experimental study. *Phys. Fluids* 9:1277–86

Campbell TA, Koster JN. 1994. Visualization of liquid-solid interface morphologies in gallium subject to natural convection. *J. Cryst. Growth* 140:414–25

Campbell TA, Koster JN. 1997. In situ visualization of constitutional supercooling within a Bridgman-Stockbarger system. *J. Cryst. Growth* 171:1–11

Cao Z-H, Xie J-C, Tang Z-M, Hu W-R. 1992. Experimental study on oscillatory thermocapillary convection. *Sci. China Ser. A* 35:725–33

Carotenuto L, Castagnolo D, Albanese C, Monti R. 1998. Instability of thermocapillary convection in liquid bridges. *Phys. Fluids* 10:555–65

Cerisier P, Jamond C, Pantaloni J, Charmet JC. 1984. Surface relief in Bénard-Marangoni convection. *J. Phys.* (*France*) 45:405–11

Cerisier P, Jamond C, Pantaloni J, Pérez-García C. 1987a. Stability of roll and hexagonal patterns in Bénard-Marangoni convection. *Phys. Fluids* 30:954–59

Cerisier P, Occelli R, Pérez-García C, Jamond C. 1987b. Structural disorder in Bénard-Marangoni convection. *J. Phys.* (*France*) 48:569–76

Cerisier P, Pérez-García C, Occelli R. 1993. Evolution of induced patterns in surface-tension-driven Bénard convection. *Phys. Rev. E* 47:3316–25

Cerisier P, Rahal S, Billia B. 1996a. Extrinsic effects on the disorder dynamics of Bénard-Marangoni patterns. *Phys. Rev. E* 54:3508–17

Cerisier P, Rahal S, Rivier N. 1996b. Topological correlations in Bénard-Marangoni convective structures. *Phys. Rev. E* 54:5086–94

Chun C-H. 1980. Marangoni convection in a floating zone under reduced gravity. *J. Cryst. Growth* 48:600–10

Chun C-H, Wuest W. 1979. Experiments on the transition from the steady to the oscillatory Marangoni-convection of a floating zone under reduced gravity effect. *Acta Astron.* 6:1073–82

Chun C-H, Wuest W. 1982. Suppression of temperature oscillations of thermal Marangoni convection in a floating zone by superimposing of rotating flows. *Acta Astron.* 9:225–30

Ciliberto S, Coullet P, Lega J, Pampaloni E, Pérez-García C. 1990. Defects in roll-hexagon competition. *Phys. Rev. Lett.* 65:2370–73

Cross MC, Hohenberg PC. 1993. Pattern formation outside of equilibrium. *Rev. Mod. Phys.* 65:851–1112

Dauby PC, Lebon G. 1996. Bénard-Marangoni instability in rigid rectangular containers. *J. Fluid Mech.* 329:25–64

Daviaud F, Vince JM. 1993. Traveling waves in a fluid layer subjected to a horizontal temperature gradient. *Phys. Rev. E* 48:4432–36

Davis SH. 1987. Thermocapillary instabilities. *Annu. Rev. Fluid Mech.* 19:403–35

Davis SH, Homsy GM. 1980. Energy stability theory for free-surface problems: buoyancy-thermocapillary layers. *J. Fluid Mech.* 98:527–53

Dell'Aversana P, Neitzel GP. 1998. When liquids stay dry. *Phys. Today* 51:38–41

Dell'Aversana P, Tontodonato V, Carotenuto L. 1997. Suppression of coalescence and wetting: the shape of the interstitial film. *Phys. Fluids* 9:2475–85

De Saedeleer C, Garcimartin A, Chavepeyer G, Platten JK. 1996. The instability of a liquid layer heated from the side when the upper surface is open to air. *Phys. Fluids* 8:670–76

DiPrima RC, Swinney HL. 1981. Instabilities and transition in flow between concentric rotating cylinders. In *Hydrodynamic Instabilities and the Transition to Turbulence* , ed. HL Swinney, JP Gollub, pp. 139–80. Berlin: Springer-Verlag

Dupont O, Hennenberg M, Legros JC. 1992. Marangoni-Bénard instabilities under non-steady conditions. Experimental and theoretical results. *Int. J. Heat Mass Transf.* 35:3237–44

Eckert K, Bestehorn M, Thess A. 1998. Square

cells in surface-tension-driven Bénard convection: experiment and theory. *J. Fluid Mech.* 356:155–97

Eyer A, Leiste H, Nitsche R. 1985. Floating-zone growth of silicon under microgravity in a sounding rocket. *J. Cryst. Growth* 71:173–82

Ezersky AB, Garcimartin A, Burguete J, Mancini HL, Pérez-García C. 1993. Hydrothermal waves in Marangoni convection in a cylindrical container. *Phys. Rev. E* 47:1126–31

Frank S, Schwabe D. 1997. Temporal and spatial elements of thermocapillary convection in floating zones. *Exp. Fluids* 23:234–51

Gatos HC. 1982. Semiconductor crystal growth and segregation problems on earth and in space. In *Materials Processing in the Reduced Gravity Environment of Space,* ed. GE Rindone, pp. 355–71. Amsterdam: Elsevier

Gillon P, Homsy GM. 1996. Combined thermocapillary-buoyancy convection in a cavity: an experimental study. *Phys. Fluids* 8:2953–63

Golovin AA, Nepomnyashchy AA, Pisman LM. 1997. Nonlinear evolution and secondary instabilities of Marangoni convection in a liquid-gas system with deformable interface. *J. Fluid Mech.* 341:317–41

Han JH, Sun ZW, Dai LR, Xie JC, Hu WR. 1996. Experiment on the thermocapillary convection of a mercury liquid bridge in a floating half zone. *J. Cryst. Growth* 169:129–35

Hibiya T, Nakamura S, Imaishi N, Mukai K, Onuma K, et al. 1998. Marangoni flow of Si melt: microgravity experiments and perspective. *J. Jpn. Soc. Microgravity Appl.* 15:399–406

Hu WR, Shu JZ, Zhou R, Tang ZM. 1994. Influence of liquid bridge volume on the onset of oscillation in floating zone convection: I. Experiments. *J. Cryst. Growth* 142:379–84

Jeffreys H. 1951. The surface elevation on cellular convection. *Q. J. Mech. Appl. Math.* 4:283–88

Jurisch M. 1990. Surface temperature oscillations of a floating zone resulting from oscillatory thermocapillary convection. *J. Cryst. Growth* 102:223–32

Kamotani Y, Kim J. 1988. Effect of zone rotation on oscillatory thermocapillary flow in simulated floating zones. *J. Cryst. Growth* 87:62–68

Kamotani Y, Lee JH, Ostrach S. 1992. An experimental study of oscillatory thermocapillary convection in cylindrical containers. *Phys. Fluids A* 4:955–62

Koschmieder EL, Biggerstaff MI. 1986. Onset of surface-tension-driven Bénard convection. *J. Fluid Mech.* 167:49–64

Koschmieder EL, Prahl SA. 1990. Surface-tension-driven Bénard convection in small containers. *J. Fluid Mech.* 215:571–83

Koschmieder EL, Switzer DW. 1992. The wavenumbers of surface-tension-driven Bénard convection. *J. Fluid Mech.* 240:533–48

Lavalley R, Amberg G, Alfredsson H. 2001. Experimental and numerical investigations of nonlinear thermocapillary oscillations. *Eur. J. Mech. B.* Submitted

Levenstam M, Amberg G, Carlberg T, Andersson M. 1996. Experimental and numerical studies of thermocapillary convection in a floating zone like configuration. *J. Cryst. Growth* 158:224–30

Monti R, Castagnolo D, Dell'Aversana P, Desiderio G, Moreno S, et al. 1992. An experimental and numerical analysis of thermocapillary flow of silicone oils in a microfloating zone. *43rd Congr. Int. Astron. Fed.,* Washington, DC

Muehlner KA, Schatz MF, Petrov V, McCormick WD, Swift JB, et al. 1997. Observation of helical traveling-wave convection in a liquid bridge. *Phys. Fluids* 9:1850–52

Mundrane M, Zebib A. 1993. Two- and three-dimensional buoyant-thermocapillary convection. *Phys. Fluids A* 5:810–18

Nakamura S, Hibiya T, Imaishi N, Yoda S-I, Nakamura T, et al. 1999. Observation of

periodic Marangoni convection in a molten silicon bridge on board the TR-IA-6 rocket. *J. Jpn. Soc. Microgravity Appl.* 16:99–103

Nitschke K, Thess A. 1995. Secondary instability in surface-tension-driven Bénard convection. *Phys. Rev. E* 52:R5772–75

Occelli R, Guazzelli E, Pantaloni J. 1983. Order in convection structures. *J. Physique–Lettres* 44:L-567–80

Ondarçuhu T, Millan-Rodriguez J, Mancini HL, Garcimartin A, Pérez-García C. 1993a. Bénard-Marangoni convective patterns in small cylindrical layers. *Phys. Rev. E* 48:1051–57

Ondarçuhu T, Mindlin G, Mancini HL, Pérez-García C. 1993b. Dynamical patterns in Bénard-Marangoni convection in a square container. *Phys. Rev. Lett.* 70:3892–95

Ondarçuhu T, Mindlin G, Mancini HL, Pérez-García C. 1994. The chaotic evolution of patterns in Bénard-Marangoni convection with square symmetry. *J. Phys. Condens. Matter* 6:A427–32

Or AC, Kelly RE, Cortelezzi L, Speyer JL. 1999. Control of long-wavelength Marangoni-Bénard convection. *J. Fluid Mech.* 387:321–41

Pearson JRA. 1958. On convection cells induced by surface tension. *J. Fluid Mech.* 4:489–500

Pérez-García C, Echebarria B, Bestehorn M. 1998. Thermal properties in surface-tension-driven convection. *Phys. Rev. E* 57:475–81

Pérez-García C, Pantaloni J, Occelli R, Cerisier P. 1985. Linear analysis of surface deflection in Bénard-Marangoni instability. *J. Phys.* (*France*) 46:2047–51

Petrov V, Haaning A, Muehlner KA, VanHook SJ, Swinney HL. 1998. Model-independent nonlinear control algorithm with application to a liquid bridge experiment. *Phys. Rev. E* 58:427–33

Petrov V, Schatz MF, Muehlner KA, VanHook SJ, McCormick WD, et al. 1996. Nonlinear control of remote unstable states in a liquid bridge convection. *Phys. Rev. Lett.* 77:3779–82

Pool RE, Koster JN. 1994. Visualization of density fields in liquid metals. *Int. J. Heat Mass Transf.* 37:2583–87

Preisser F, Schwabe D, Scharmann A. 1983. Steady and oscillatory thermocapillary convection in liquid columns with free cylindrical surface. *J. Fluid Mech.* 126:545–67

Riley RJ, Neitzel GP. 1998. Instability of thermocapillary-buoyancy convection in shallow layers. Part 1. Characterization of steady and oscillatory instabilities. *J. Fluid Mech.* 359:143–64

Scanlon JW, Segal LA. 1967. Finite amplitude cellular convection induced by surface tension. *J. Fluid Mech.* 30:149–62

Schatz MF, Howden K. 1995. Purification of silicone oils for fluid experiments. *Exp. Fluids* 19:359–61

Schatz MF, VanHook SJ, McCormick WD, Swift JB, Swinney HL. 1995. Onset of surface-tension-driven Bénard convection. *Phys. Rev. Lett.* 75:1938–41

Schatz MF, VanHook SJ, McCormick WD, Swift JB, Swinney HL. 1999. Time-independent square patterns in surface-tension-driven Bénard convection. *Phys. Fluids* 11:2577–82

Schwabe D. 1981. Marangoni effects in crystal growth melts. *PhysicoChem. Hydrodyn.* 2:263–80

Schwabe D, Möller U, Schneider J, Scharmann A. 1992. Instabilities of shallow dynamic thermocapillary liquid layers. *Phys. Fluids A* 4:2368–81

Schwabe D, Preisser F, Scharmann A. 1982. Verification of the oscillatory state of thermocapillary convection in a floating zone under low gravity. *Acta Astron.* 9:265–73

Schwabe D, Scharmann A. 1985. Messung der kritischen Marangonizahl für den Übergang von stationärer zu oszillatorischer thermokapillarer Konvektion unter mikrogravitation: ergebnisse der experimente in den ballistischen Raketen TEXUS 5 und TEXUS 8. *Z. Flugwiss. Weltraumforsch.* 9:21–28

Schwabe D, Velten R, Scharmann A. 1990. The

instability of surface tension driven flow in models for floating zones under normal and reduced gravity. *J. Cryst. Growth* 99:1258–64

Scriven LE, Sternling CV. 1960. The Marangoni effects. *Nature* 187:186–88

Shevtsova VM, Legros J-C. 1998. Oscillatory convective motion in deformed liquid bridges. *Phys. Fluids* 10:1621–34

Shu JZ, Yao YL, Zhou R, Hu WR. 1994. Experimental study of free surface oscillations of a liquid bridge by optical diagnostics. *Microgravity Sci. Technol.* 7:83–89

Smith MK. 1986. Instability mechanisms in dynamic thermocapillary liquid layers. *Phys. Fluids* 29:3182–86

Smith MK, Davis SH. 1983. Instabilities of dynamic thermocapillary liquid layers. Part 1. Convective instabilities. *J. Fluid Mech.* 132:119–44

Sumner LBS, Neitzel GP. 2001. Oscillatory thermocapillary convection in liquid bridges with highly deformed free surfaces. Experiments and energy-stability analysis. *Phys. Fluids.* In press

VanHook SJ, Schatz MF, Swift JB, McCormick WD, Swinney HL. 1995. Long-wavelength instability in surface-tension-driven Bénard convection. *Phys. Rev. Lett.* 75:4397–400

VanHook SJ, Schatz MF, Swift JB, McCormick WD, Swinney HL. 1997. Long-wavelength surface-tension-driven Bénard convection: experiment and theory. *J. Fluid Mech.* 345:45–78

Velten R, Schwabe D, Scharmann A. 1991. The periodic instability of thermocapillary convection in cylindrical liquid bridges. *Phys. Fluids A* 3:267–79

Villers D, Platten JK. 1992. Coupled buoyancy and Marangoni convection in acetone: experiments and comparison with numerical simulations. *J. Fluid Mech.* 224:487–510

Wilson SK, Thess A. 1997. On the linear growth rates of the long-wave modes in Bénard-Marangoni convection. *Phys. Fluids* 9:2455–57

Xu J-J, Davis SH. 1984. Convective thermocapillary instabilities in liquid bridges. *Phys. Fluids* 27:1102–7

Yao YL, Shu JZ, Xie JC, Liu F, Hu WR, et al. 1997. Transition of oscillatory floating half-zone convection from Earth's gravity to microgravity. *Int. J. Heat Mass Transf.* 40:2517–24

Robert Legendre

Henri Werlé

Annual Review of Fluid Mechanics
Volume 33, 2001

CONTENTS